Elevated temperature contact creep and friction of nickel-based superalloys using machine learning assisted finite element analysis

Sepehr Salari[a], Farnaz Behnia[b], Andreas A. Polycarpou[c], Ali Beheshti[a,*]

[a] Department of Mechanical Engineering, George Mason University, Fairfax, VA, 22030, USA

[b] Department of Systems Engineering and Operations Research, George Mason University, Fairfax, VA, 22030, USA

[c] J. Mike Walker Department of Mechanical Engineering, Texas A&M University, College Station, TX, 77843, USA

Abstract

Nickel-based superalloys with superior thermochemical, mechanical, and tribological properties are highly utilized for critical components in several high temperature applications such as gas turbines and nuclear reactors. Inconel 617, in particular, is considered as one of the main candidate superalloys for tribo-components in very-high-temperature gas-cooled nuclear reactors. Recent findings indicate that this alloy grows unique surface oxide especially in a high-temperature helium environment with distinctive wear, friction, and contact properties. This study investigates the high temperature contact area evolution and frictional behavior of Inconel 617 using finite element simulation and provides predictive models for the contact and friction performance at different normal loads, dwell times, and temperatures. High temperature helium-aged Inconel 617 top surface properties (up to 600 °C) are utilized along with a single asperity-based deformable elastic-plastic contact model under combined normal and tangential loading. Machine learning is used to assist the finite element results and to predict friction coefficient as well as contact area evolution. While a small difference is observed in the instantaneous friction coefficient (no dwell time) for all temperatures, friction coefficient increases considerably with dwell time. This shows that the effect of contact creep for longer dwell times significantly dominants the effect of high temperature variation in basic mechanical parameters such as modulus and yield strength. It is found that increasing temperature and dwell times lead to the friction coefficient increase, yet the dominance of dwell time effects decreases at higher temperatures and loads. While the analysis is presented for Inconel 617, the methodology is easy to be generalized and can be applied to other HT alloys.

***Keywords**: Superalloys; Elastic-Plastic-Viscoplastic Contact; High Temperatures; Static Friction; Machine Learning; Artificial Neural Network*

1. Introduction

In view of design demands, providing materials that can withstand high temperature (HT) and its concomitant HT creep deformation, is vital for the effective and reliable operation of mechanical components. Advanced nuclear reactors (Wright, 2006a), jet engines (Klocke et al., 2013), and gas turbines are among several applications that HT creep deformation severely affects their

* Tel.: +1-703-993-5638; E-*mail address*: abehesh@gmu.edu (Ali Beheshti).

performance. Inconel 617 (symbolized as IN617, hereinafter) is one of the advanced materials to enable higher operating temperatures for many HT applications. In particular, it is among the main candidate materials for next-generation very-high temperature reactors (VHTR) and high-temperature gas-cooled reactors (HTGR) due to its excellent mechanical and chemical properties as well as surface stability. It is mostly to be utilized for controlling rods, valves, and other contacting pairs in Gen. IV reactors (Cabet et al., 2006; Wright, 2006b, 2006a). Operating under HT and often long idle conditions, however, makes them suspectable to contact and tribological challenges (Salari et al., 2022). When it comes to the mechanical contacts and interfaces, the surface of these components is not perfectly smooth, and contact occurs at small discrete areas (asperity tips). These microscopic asperities with small contact areas and usually under high contact stress give rise to the likelihood of contact creep deformation (Feng and Ngan, 2002). Creep of these contacting asperities relaxes contact stress, increases contact strain, and subsequently expands the overall contact area. This, in turn, results in a considerable change at the micro and subsequently macro scales contact and frictional behaviors. This is significant for the reliable performance and predictable longevity of several reactor mission-critical components. For instance, this can adversely affect the precise motion of controlling rods in nuclear reactors (Stanford, 2007). In fact, HT contact creep and self-welding during long idle intervals causes unpredictable high static friction and often surface damage (Zheng et al., 2020). The extent of static friction and its predictability is of particular concern for the design and maintenance as well as control and actuation operations since the material pairs experience high temperatures and high loads under intermittent movements with long dwell times significantly affecting frictional and contact behavior (Stanford, 2007).

Static coefficient of friction (referred to as COF, hereinafter) and sliding inception phenomena have been studied since the pioneering work of Coulomb (1785). He proposed a constant COF being basically the proportionality factor between tangential load and normal load at the sliding inception. Mindlin developed a COF formula for a spherical contact with elastic Hertzian normal pressure following the Coulomb friction model: assuming sliding occurs when the entire surface points reach the shear limit (Mindlin, and Deresiewicz, 1953). Tabor later suggested adhesion and shear strength of the contact as well as the real contact area as the main elements influencing the COF (Tabor, 1981). Chang et al. incorporated these elements in their model, and calculated the friction force of a single asperity while assuming yielding inception as a criterion (Chang et al., 1988). Using finite element (FE), a semi-analytical solution was developed by Kogut and

Etsion (KE model) to provide an empirical expression for the COF of a single asperity based on the initiation of the yield in the softer component (Kogut and Etsion, 2003). Etsion and his colleagues (BKE model) later suggested a new approach for determining the sliding inception by defining relative contact stiffness and considering the contact in full stick condition (Brizmer et al., 2007). Later, a sliding criterion was developed by Polycarpou and his coworkers (WSP model) assuming that sliding occurs when shear stress at all contacting points reaches material bulk maximum shear strength (Wu et al., 2012). Their proposed model was shown to be accurate for a wider range of loads covering both the KE (low interference) and BKE (high interferences) models (Wu et al., 2012).

Early efforts to describe the observed time dependency of COF suggested it's linked to creep deformation of asperities at micro-scales (Moore and Tabor, 1952; Rabinowicz and Tanner, 1966; Spurr, 1955). These studies showed an increase in the contact area with dwell time, which may explain COF increase. However, owing to the multitude of factors influencing the mechanism, detailed contribution of creep deformation on the sliding inception behavior was not established. In another study, Malamut et al. (MKE model) numerically studied the effect of dwell time and normal load on static friction of a creeping elastic-plastic PTFE hemispherical contact (Malamut et al., 2009). Based on their findings, in addition to the increase in the contact area, an increase in initial tangential stiffness due to stress relaxation at the contact significantly influences the tangential load, and consequently, the COF (Malamut et al., 2009). Based on their best-fit curves to the FE simulations, Malamut et al. suggested an empirical COF for a polymer-based single asperity at any dwell time and a range of normal loads at room temperature (Malamut et al., 2009). This model was further evaluated by the experimental work of Kasem et al. who performed a set of experiments using PTFE spheres to study the effect of dwell time, normal load, and spherical diameter on the COF (Kasem and Etsion, 2014). Experimental results showed a comparable course of evolution for COF in comparison to the FE results of MKE in which COF increases with the dwell time (Kasem and Etsion, 2014; Malamut et al., 2009). It is worth mentioning that regarding rough surface contact creep, a few attempts were made on studying friction behavior and the electro-mechanical response of the surface using, for example, the fractal representation of the surface (see Refs. (Goedecke and Mock, 2010; Rezvanian et al., 2008)). For a comprehensive review of contact and friction creep studies, the reader is referred to the recent review by the authors (Salari and Beheshti, 2021).

The above-mentioned models described COF evolution for a variety of loads, dwell times, and material properties, yet a predictive model for contact and friction behavior to incorporate these parameters, especially, along with temperature variation is lacking in the literature. While this predictive model is highly beneficial for several HT contact applications, the shortcoming might be related to the intricacies associated with the development of a comprehensive numerical and predictive model with complex nonlinearity over wide length, temperature as well as time scales. The problem, however, can be potentially addressed with the advent of powerful computers and the FE technique as well as the utilization of advanced machine learning (ML) tools such as artificial neural networks (ANNs or for simplicity NNs) (Behnia et al., 2020; Deng and Li, 2013; He et al., 2016; Heidari et al., 2021; Kingma and Ba, 2014; Kumar et al., 2016).

Recently, mechanical engineering and, in particular, the tribology community have started to realize the advantages and efficacy of ML techniques. For example, Thankachan et al. employed a regression model for optimizing the tribological behavior of hybrid copper surface composites (Thankachan et al., 2018) whereas Borjali et al. generated a data-driven model that allowed the prediction of polyethylene wear rate based on several operating parameters (Borjali et al., 2019). The above attempts showed that NNs-based models can potentially reduce the need for experimental studies and can also be used to validate the new experimental data. In addition, Senatore et al. presented a comprehensive view of the main sliding parameters influencing brake and clutch friction and sliding motion using the NNs method (Senatore et al., 2011). Sattari et al. developed a machine learning method to predict the intrinsic friction of 2D lubricants by measuring the surface maximum energy barrier for 2D materials having different structural, electrical, chemical, thermal and mechanical properties (Sattari Baboukani et al., 2020). NNs-based constitutive models are other applications of NNs which were used along FE simulations. Unlike the conventional implementation of plasticity models, NNs do not require special integration procedures for implementation in FE analysis (Hashash et al., 2004). In another study, multiple welding parameters were studied using NNs to predict the tensile strength, hardness, and percentage of elongation of the welded alloys (Khourshid et al., n.d.). A review on advances at the intersection of data science with mechanical deformation simulations has been presented by Frydrych et al. (Frydrych et al., 2021). The NNs algorithms have also shown the sensitivity of each input parameter and its influence on the studied parameter for these studies. It

is evident that ML algorithms are powerful tools to provide a simple prediction model and are highly flexible to incorporate different parameters.

Let's now turn our attention to tribological components in HTGR/VHTR applications. Due to the presence of Helium (He) as a coolant with inevitable impurities, the metallic alloys (e.g., IN617) develop unique surface oxides which significantly influence surface friction, wear, and contact properties and in turn, impact the performance of the components (Sakaba et al., 2010). In the authors' previous study, the time-independent and dependent mechanical properties of the oxide were studied (Salari et al., 2020). Particularly, creep characterization and mechanical parameters of the oxide under indentation were investigated and extracted. Results showed that while Young's modulus of the oxide is relatively close to the bulk of IN617 for temperatures up to 600°C, the yield strength, and hardness, in comparison to the bulk material, increase significantly due to oxidation of the IN617 after aging. The calculated creep parameters, as well as activation energy, showed that creep of the oxide depends on the diffusion through the grains, unlike the bulk material in which the main creep mechanism is dislocation climb (Salari et al., 2020; Zhang et al., 2017). The elevated temperature surface material properties exclusively extracted for He-aged IN617 by the authors (reported in (Salari et al., 2020)) are used here to model and predict IN617 oxide contact and COF response at elevated temperatures.

The current study investigates the HT contact area and frictional characteristics of a single asperity from room temperature to 600 °C for the IN617 surface with the assistance of FE analysis. While this method is presented for the specific material of interest (which its mechanical properties were extracted from our previous study (Salari et al., 2020)), the methodology can be applied to other HT alloys and is easy to be generalized. Final simulated contact area and COF results are used as input data points for a NN algorithm to introduce comprehensive predictive models based on input values of temperature, load, and dwell time. While the focus of this study is on modeling HT contact creep and friction, the NNs approach was used as a powerful tool to come up with an easy-to-use and extendable model and also show the capability of NN to the mechanics and materials and in particular contact mechanics and tribology community. Additionally, similar to the MLK, empirical relations for the COF and contact area (details in Supplementary Information, SI) are introduced and their accuracy are compared to the NNs.

2. Finite element model

In this work, a FE model, within ABAQUS® 2020, was adopted to develop a three-dimensional deformable hemisphere in contact with a rigid flat surface (flattening model). The contact was analyzed with an implicit solver for the normal pre-load (first step) and tangential loading (last step) while a quasi-static approach was chosen to analyze the time-dependent material response (intermediate step) assuming negligible inertia effects (Smith, 2017).

Elastic-plastic-viscoplastic with work hardening properties were assumed for the deformable hemisphere following authors' previous HT indentation study (Salari et al., 2020) on IN617. Adopting properties obtained from common uniaxial creep test in the literature is not available for IN617 oxide and more importantly, even if available for a material, mechanical properties based on indentation creep are more reliable in analyzing contact creep flattening. Hence, all the material properties here are based on our previous measurements (indentation creep) on the oxide surface of aged IN617 (Table 1) (Salari et al., 2020) where IN617 were aged at 950 °C for 100 hours in He to simulate the He-cooled reactor environment. In that study, nanoindentation on the cross-section of the oxide was carried out from room temperature up to 600 °C and load-displacement, as well as creep displacement evolution with time, were obtained. For these measurements, hardness size effect is an important factor to be considered. Based on the extracted hardness and discussion available in Ref. (Salari et al., 2020), consistent results were observed for different loads and temperatures. The extracted results were also validated with other metal oxides in Ref. (Salari et al., 2020) showing good agreements. Following a work hardening model as well as a power-law creep (see Eqs. 1 and 2), raw experimental graphs along with complimentary iterative FE simulations were utilized to obtain the mechanical properties at different temperatures including Youngs' modulus (E), Poisson's ratio (ν), yield strength (σ_y), and strain work hardening exponent (n_1). Additionally, time-dependent properties were calculated including creep coefficient (A) and creep exponent (n_2). For full details please see Ref. (Salari et al., 2020).

$$\sigma_f = \sigma_y\left(1 + \frac{E\times\varepsilon_p}{\sigma_y}\right)^{n_1} \quad (1)$$

$$\dot{\varepsilon} = A\sigma^{n_2} \quad (2)$$

In Eqs. 1 and 2, σ_f and ε_p denote the flow stress and strain, respectively and $\dot{\varepsilon}$ is the creep strain rate.

Table 1 Mechanical properties of oxide surface of aged Inconel 617 (Salari et al., 2020).

Temperature (°C)	E (GPa)	ν	σ_y (GPa)	n_1	A	n_2
25	294.55	0.25	10.28	0.34	3.13E-13	1.71
200	296.10	0.25	6.02	0.22	5.33E-13	1.97
400	297.81	0.25	2.60	0.18	4.75E-12	2.14
600	175.37	0.25	0.13	0.02	1.32E-09	3.51

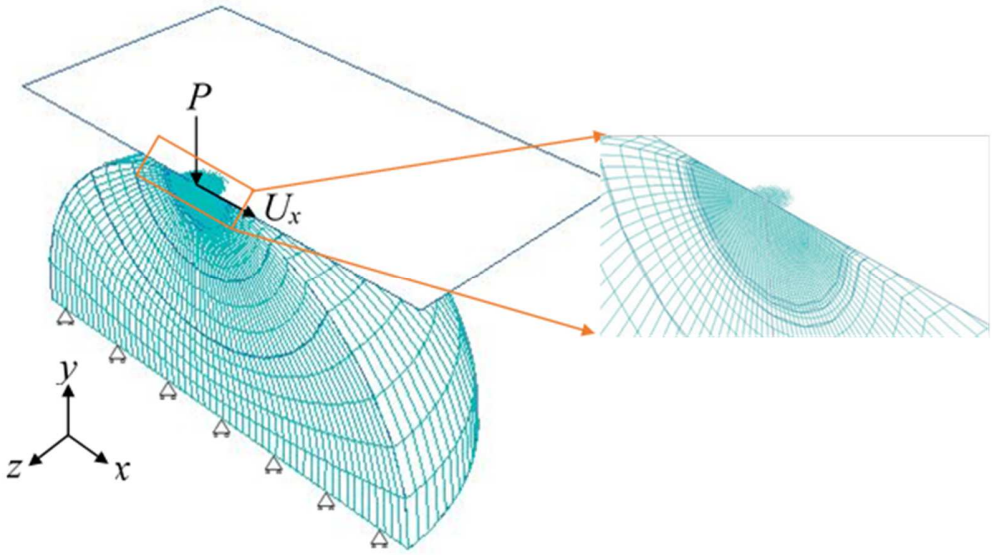

Fig. 1 *Schematic representation of the boundary condition and adopted mesh for the hemisphere at the contact.*

To reduce computer cost only half of a hemisphere was modeled and meshed with a total of 75,000 elements of reduced eight-node hexahedral, C3D8R, as shown in **Fig. 1**. The hemisphere, with a radius of $R = 1\,mm$, was divided into multiple regions to have a gradual mesh size increase from the contact region. The finest elements were selected near the contact area where their size was 0.002 times the elements at the bottom to get consistent results for the stress, creep strain, and contact area. The deformable hemisphere was fully contained at the bottom, and a symmetry boundary condition was applied for the symmetry plane. Different normal loads were applied on the rigid flat in the normal direction (y) followed by a holding period with a range of different dwell times, t_d, from 0 (instantaneous) to 1000 minutes while the load was kept

constant. For generalization, here we use nondimensional normal load as $P^* = {}^{L}/_{L_c}$ where normal load, L, is nondimensionalized with respect to the critical normal load (L_c) beyond which the contact is no longer elastic. Based on Hertzian solution, L_c, its associated critical interference, ω_c, and critical contact area, A_c, at the onset of yielding are given by:

$$L_c = \frac{4}{3} E^* R^{0.5} \omega_c^{1.5} \tag{3}$$

$$\omega_c = \left(\frac{\pi k H}{2E^*}\right)^2 R \tag{4}$$

$$A_c = \pi R \omega_c \tag{5}$$

where

$$E^* = \frac{E_i}{1 - \nu_i^2} \tag{6}$$

subscript i relates to IN617 as the elastic modulus for the rigid flat is assumed to be infinity. H represents the hardness and k is the proportionality factor between the maximum contact pressure and the hardness at the onset of plastic deformation. Kogut and Etsion proposed a relationship ($k = 0.454 + 0.41\nu$) for the calculation of k. Here, based on the measured average Poisson value (0.25) for IN617 oxide, k was taken equal to 0.55. The range of P^* (0.5 to 11) and t_d (0 to 1000 minutes) were chosen such way that they cover wide deformation regimes—elastic (before yielding) to high plastic regimes—and time-dependent creep deformations. It should be added that due to large deformations, numerical convergence for higher load values and especially under long dwell times was challenging, however, whenever possible the load was increased up to $P^* = 16$. It should be noted that one of the main benefits of single asperity contact models is their ability to be expanded to rough surface models e.g., Greenwood and Williamson (GW) based models, simulating entire contact behaviors (Greenwood et al., 1966). However, asperity interaction and most importantly asperity merging are not generally valid in GW based models and, hence, deformation of an asperity beyond threshold value of $\lambda = {}^{a}/_{R} \sim$ 0.4 (a is the radius of contact area) is not typically considered in asperity contact models (Beheshti and Khonsari, 2014, 2012; Jackson and Green, 2005). Accordingly, here, the simulations were stopped at large values of λ (more than 0.4). It is believed that beyond this threshold asperities are not deformed independently and for many tribological applications, it is either unlikely or unacceptable (Greenwood et al., 1966; Jackson and Green, 2005).

Here, first normal load P^* was applied to the contact followed by the holding period (t_d). Subsequently, a ramp displacement loading (U_x) was applied in the tangential direction (x) until "sliding" occurred. The friction for the normal loading is assumed to be negligible (Eriten et al., 2012), however, for the tangential displacement, a very large local COF was selected for the entire contact following WSP partial slip approach (Wu et al., 2012) so the input local COF did not serve as a threshold. Rather, in the WSP model, critical maximum frictional shear stress, τ_c, was used as the criterion for the local sliding inception. $\tau_c = {\sigma_y}/{\sqrt{3}}$ was selected as contact maximum shear stress where σ_y denotes the yield strength of the material under investigation (here, it is the aged IN617 surface yield strength at 25 °C to 600 °C (Salari et al., 2020)). Per the WSP model, "sliding" happens when shear stress on the entire contact reaches τ_c. WSP model was shown to be valid over large normal interference ranges covering both the KE and the BKE models (Brizmer et al., 2007).

Another important computational parameter for the tangential loading step is the elastic slip (ES) which should be adjusted for implicit solvers to get converged solution. ES is an elastic displacement during the stick period that may induce additional elastic slip during tangential loading (Smith, 2017). It should be mentioned that lower values of ES may give accurate results, however, the simulations are not computationally efficient. Therefore, to reach the optimum value for ES, the current FE model was compared and verified against the results reported by the WSP and MKE models for multiple holding durations and displacements (Malamut et al., 2009; Wu et al., 2012). Based on the outcome, a value of 0.002 was selected for ES for which the estimated friction force fell within 5% of WSP and MKE models (Malamut et al., 2009; Wu et al., 2012). The maximum corresponding tangential load at sliding inception is considered as Q_{max} and, hence, the COF equals Q_{max} divided by the constant normal load. In addition the numerical model requires "creep tolerance" parameter which is a parameter to control the accuracy of the creep integration at each load increment for the FE software and can be calculated by selecting an acceptable stress error tolerance, σ_{err}, divided by a typical elastic modulus, E (Smith, 2017). In this study, σ_{err} is taken to be $2\,MPa$. Each FE simulation took around 1 hour depending on the convergence rate. To come up with sufficient point observations for the NNs, FE results were used for extended parameters which generated around 1000 data points taking approximately 2 months.

3. Predictive neural network

As discussed above, this paper studies the superalloy contact/friction behavior through FE simulations which is, especially, the first attempt to evaluate contact creep and friction at elevated temperatures. Since the input (temperature, dwell time, and load) and the sought output (COF, contact area) parameters have a nonlinear relationship, achieving a precise comprehensive empirical expression was difficult, and therefore we employed NNs as a feasible alternative. In addition, NNs approach was utilized and introduced as a powerful tool to come up with an easy-to-use and extendable predictive model that can be applied to other tribological and contact models. Here the NNs was used to solve a "regression problem" where the output is predicting the numerical value of the target. To increase accuracy and provide enough data points for the machine learning algorithm, extensive FE simulations were carried out for random $P^*$and t_d in the range of selected parameters for the numerical analysis where final COF and contact area results were augmented to generate sufficient data points of 1000 observation points. NNs algorithms resemble the human brain in two aspects: (*i*) acquiring knowledge through a learning process, and (*ii*) storing the knowledge through connection strengths between neurons, known as nodes (Senatore et al., 2011). NNs algorithms can successfully model and predict the non-linearity of the data if suitably trained (Hahnloser et al., 2000). NNs in general consist of three or more layers. The input features are fed into the input layer, the calculations for feature extractions are done in one or more hidden layers, and finally depending on the problem, the output layer predicts or classifies the output. The nodes of each layer can be connected to the different number of nodes of the next layer. In this study, a fully connected (FC) network was used, in which every node in each layer is connected to all the nodes of the next layer. **Fig. 2** shows a simple overview of the present approach, from nanoindentation experiments of the aged oxide (Salari et al., 2020) to the flattening model and the FC neural network with an input layer of 3 nodes, one hidden layer with 13 nodes, and one output node. It should be added again, that all the material properties were based on experimental and complementary numerical analyses of IN617 nanoindentation provided in (Salari et al., 2020). These properties were used to build the FE model which was then employed to get the behavior of the friction and contact area under different load, dwell time, and temperatures. Accordingly, the data that trained NNs was all generated by the FE model. As shown in **Fig. 2** these results were then deployed and trained the

NNs. It is worth mentioning that there exists no relevant experimental study on the HT contact creep and friction.

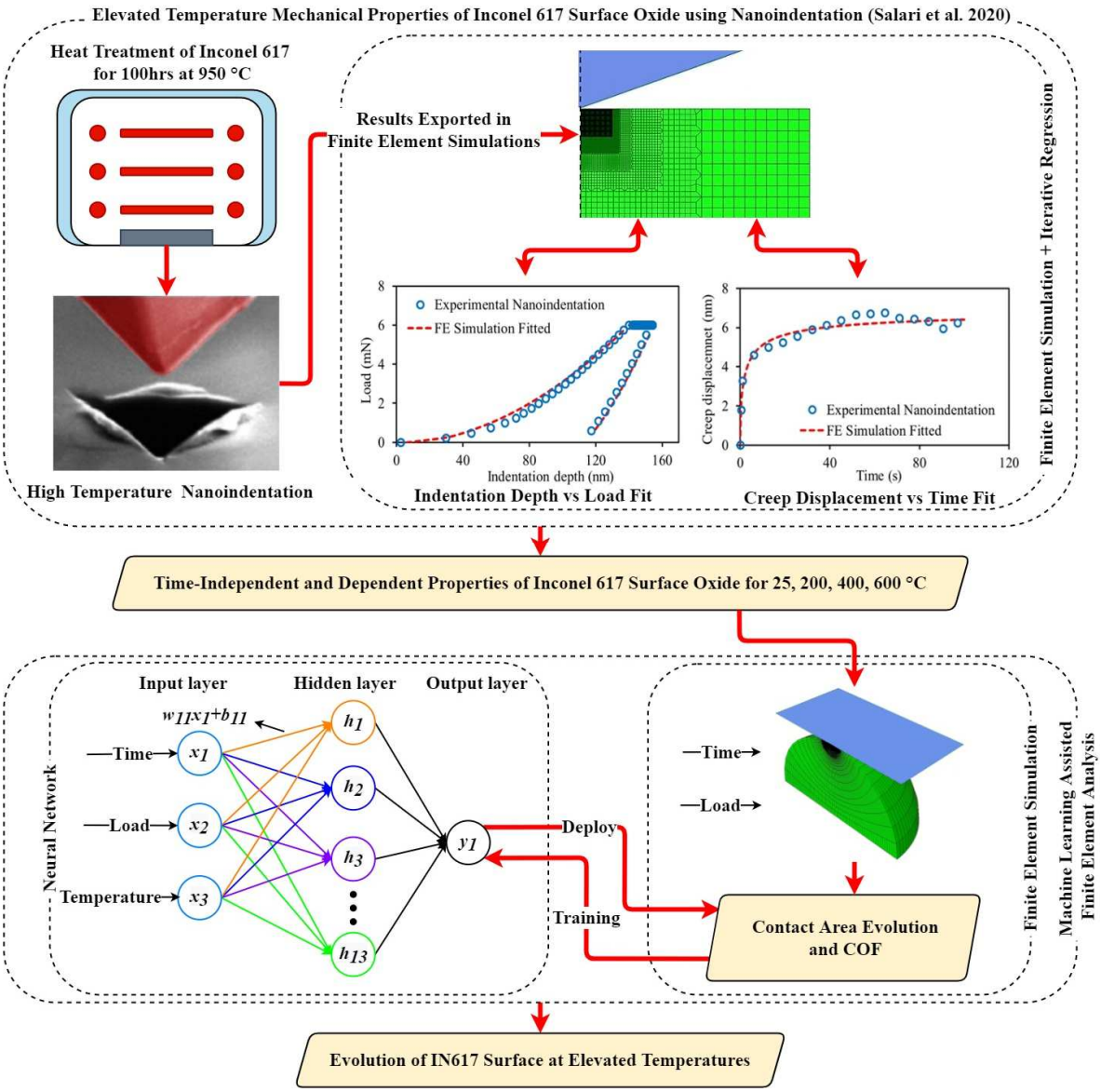

Fig. 2 *Flow chart representation of the current study from nanoindentation experiments* (Salari et al., 2020) *to the flattening FE model and the ML algorithm with a 3-layer fully connected neural network.*

In each layer, several summations and multiplications were performed to calculate the values for the next layer. The value of the j^{th} node in the n^{th} layer, h_j^n was calculated by:

$$h_j^n = \sum_{i=1}^{m} w_{ij} h_i^{n-1} + b_{ij} \tag{7}$$

where m is the number of nodes in the $(n-1)^{th}$ layer, and w_{ij} and b_{ij} respectively represent the weight and the bias of the connection. The goal of the training algorithm is to learn weights and the biases for every connection such way that the output of the network has the minimum error. However, before feeding the calculated value h_j^n to the next layer, an activation function was called to decide if the node should be activated or not. Activation functions are responsible for the nonlinearity characteristic of neural networks. Without activation functions, neural networks would be equivalent to linear regression, which may not work for many problems, especially if we anticipate our results to behave nonlinearly. Several activation functions can be utilized for different problems. In this work, the rectified linear unit (ReLU) function was employed. A ReLU function is generally defined as follows (Jain et al., 1996):

$$ReLU: f(\beta) = \begin{cases} \beta & \beta \geq 0 \\ 0 & \beta < 0 \end{cases} \tag{8}$$

where β is the output of each layer, and $f(\beta)$ is the outcome of the ReLU function, used as the input for the next layer. A loss function (also called cost or objective function) and an optimizer were required to train the neural network. Loss functions were utilized to calculate the error of the NNs output whereas the optimizer function was used to update the parameters of the network. The Mean Squared Error (MSE) loss function used in this work is given as:

$$MSE = \frac{1}{N} \sum_{i=1}^{N} (Y_i - \hat{Y}_i)^2 \tag{9}$$

where Y_i is the predicted value, $\hat{Y}_i$ is the true value, and N is the size of the test data. Here, to effectively compare the performance of the two neural networks that are trained for contact area and COF predictions, we use Eq. 10 to get the relative error (RE) of each network:

$$RE = \frac{1}{N} \sum_{i=1}^{N} \left| \frac{Y_i - \hat{Y}_i}{Y_i} \right| \tag{10}$$

The optimizer sets the policy of how the parameters of the network were updated towards the goal of optimization. For this purpose, an Adam optimizer was deployed in this work (Kingma and Ba, 2014). The run time for training our NN model was 8.89 minutes (533.201 seconds) and

the model took 0.332 seconds to predict all the test data. The summary of the NNs configuration that produces the best regression results is listed in **Table 2** and detailed code descriptions, link to the original data (based on the FE simulations) and the constants of the final NNs analysis can be found in the SI document Section S1.

Table 2 *Neural Network configuration.*

NN Type	Input size	Output size	Hidden layer/Nodes	Activation	Optimizer	Loss function
Fully Connected	3	1	1/13	ReLU	Adam	MSE

4. Results and discussion

4.1. Maximum shear stress evolution

Fig. 3 shows the evolution of dimensionless maximum shear stress, $^{\tau_{max}}/_{\tau_c}$, at the contact interface on the hemisphere along the dimensionless symmetry line as tangential load increases from zero to its max at the sliding inception. The results are depicted for dimensionless normal loads of $P^* = 0.5$ (Fig. 3a&b) and $P^* = 8$ (Figs. 3c&d) producing a fully elastic as well as elastic-plastic deformation, for $t_d = 0$ and $t_d = 100$, respectively. The shear stress distributions are depicted for the beginning of the tangential step while $Q = 0$ and when the tangential force reaches its maximum $Q = Q_{max}$ at two temperatures of 25 °C and 400 °C. For elastic normal loading and while time-dependent deformation is not significant, little difference can be observed for $^{\tau_{max}}/_{\tau_c}$ progress between two temperatures, which may relate to close time-independent elastic mechanical properties. Similar to the WSP model for the elastic deformation ($\delta_c = 0.5$) of aluminum alloy (Wu et al., 2012), before the initiation of tangential loading, the maximum shear is not at the edges of the contact and appears in the middle of the contact area, however, this is not the case after a dwell time of 100 min. It should be noted that due to the work hardening of the material (following work hardening observed in (Salari et al., 2020)), the von Mises stress (or any other equivalent stress) increases beyond the yield stress giving rise to the shear stress to go beyond the threshold at some nodes at the contact till shear stress for each node at the contact reaches τ_c. This is more evident with increased plastic deformation in which more work hardening can be seen beyond the equilibrium line $^{\tau_{max}}/_{\tau_c} = 1$. When the last node at the contact reaches τ_c, sliding initiates, and the maximum tangential force or static friction

force (Q_{max}) is recorded. This is why the maximum shear stresses shows a curved shape with the lower value points are the last node reaching the threshold criterion while the leading edges have a higher peak due to the longer history of work hardening (Wu et al., 2012).

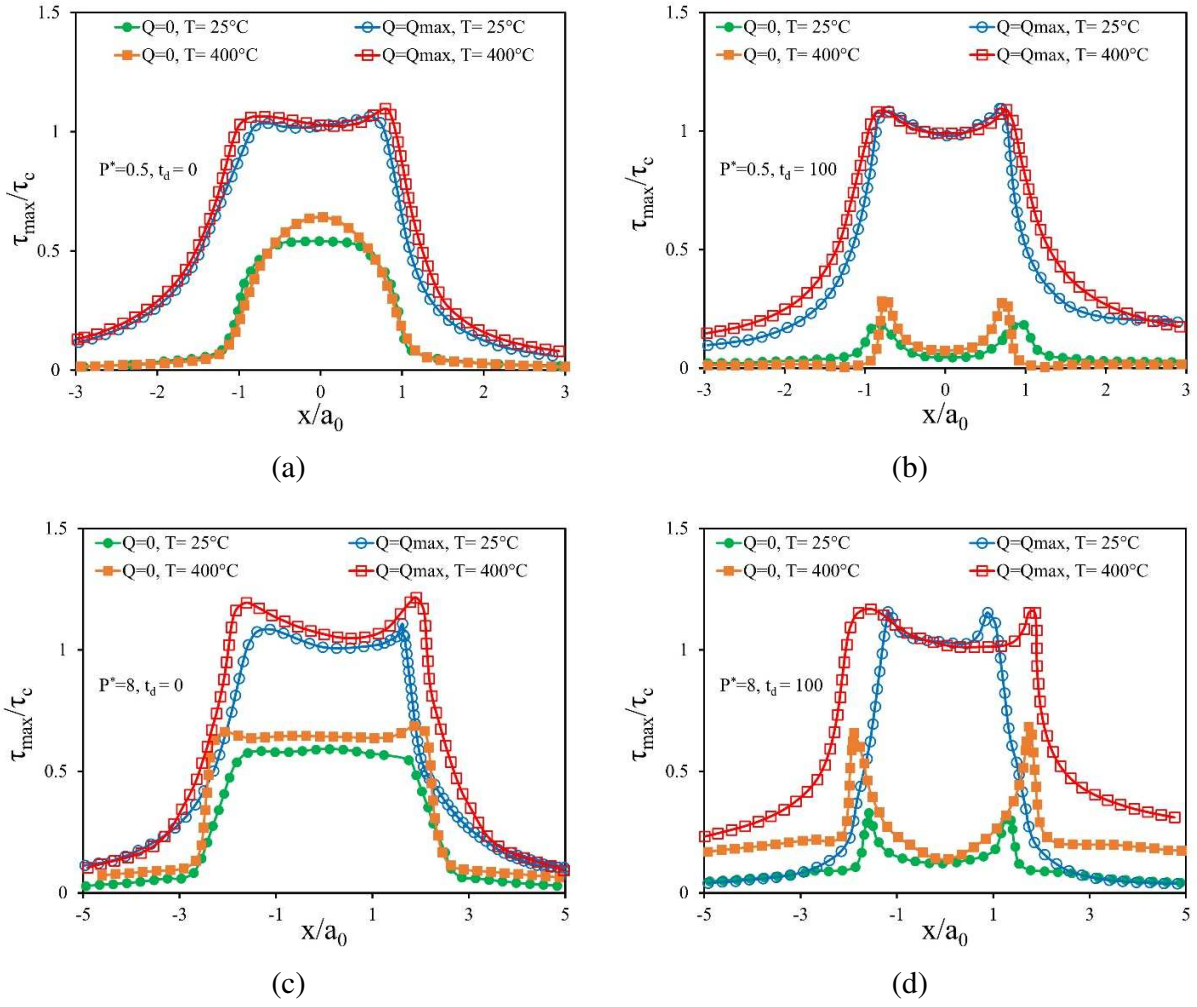

Fig. 3 *Dimensionless maximum shear stress distributions along the symmetry line on the contact area: (a&b)* $P^* = 0.5$*, and (c&d)* $P^* = 8$*,* a_0 *is the contact radius before applying tangential load.*

4.2 Time-dependent evolution of contact area and COF

Fig. 4 presents the evolution of the dimensionless normal displacement, $^{\omega}/_{\omega_0}$, where ω_0 is the interference before applying a tangential load, with dimensionless tangential displacement for two normal loads ($P^* = 0.5$ & 8) and temperatures ($T = 25$ & $400°C$). Once the load is held for a dwell time of $t_d = 100$ min, the normal displacement stays constant after applying the tangential load for both loads and temperatures. This can be related to the already expanded contact area that prohibits further expansion of the contact which is aligned with junction

growth. The embedded junction growth insets show a 12% to 18% increase for the instantaneous tangential loading ($t_d = 0$) and like normal displacement, an unnoticeable change after the dwell times, which is also reported by the FE results of MKE (Malamut et al., 2009). Based on their FE results, junction growth with tangential loading for a constant normal load of $P^* = 7$ was 27% and 13% for zero and 600 s dwell time, respectively. The reported increase in contact area is higher compare to our study (max 18%) which may relate to different material (polymer) used in the MKE study (Malamut et al., 2009; Rabinowicz and Tanner, 1966). In their work, junction growth occurs due to the need to accommodate increasing shear stress with tangential loading while maintaining the equivalent von Mises stress at the material yield strength since the mechanical properties considered as elastic- perfect plastic. In our study, due to the work hardening, the effect of junction growth decreases since there is no requirement to maintain the equivalent von Mises stress constant and it can increase with increasing strain work hardening. For the case of zero dwell time, the interference increases when reaching the plateau. Specifically for higher temperature of 400 °C and $P^* = 8$ (please note that the insets have different scales for each load and temperature). It should be noted that the detection of area growth in FE simulations is affected by relatively large errors due to the finite number of nodes in the contact interface (Goedecke and Mock, 2009).

Area growth is more noticeable during creep deformation, in which the contact area increases even after a short period resulting in stress relaxation near the contact associated with normal pressure loss. **Fig. 5** represents the evolution of von Mises stress near the contact area at 400 °C showing plastic stress initially under a load of $P^* = 8$ (Fig. 5a) whereas after a dwell time of 10 minutes the high-stress region completely disappears. Since the area under creep increases, normal pressure decreases, and subsequently, the equivalent stress at the contact falls below yield stress and, hence now even more tangential load is required to reach the same equivalent shear stress criterion (τ_c) necessary for all contact points to initiate sliding. As can be seen, the plastic zone near the contact reappeared again after the application of tangential loading (Fig. 5b). Before the creep relaxation, the center of the contact is in high contact pressure while the unaffected surrounding contained and stabilized the region. However, during the creep, this high-pressure region is no longer restricted resulting in an increase in the contact area due to the expansion of this region. During this expansion, new shear stress is created by the center material

pushing the surrounding material aside which can be recognized as peak values near the very edge of the contact line with higher von Mises stress (Fig. 3).

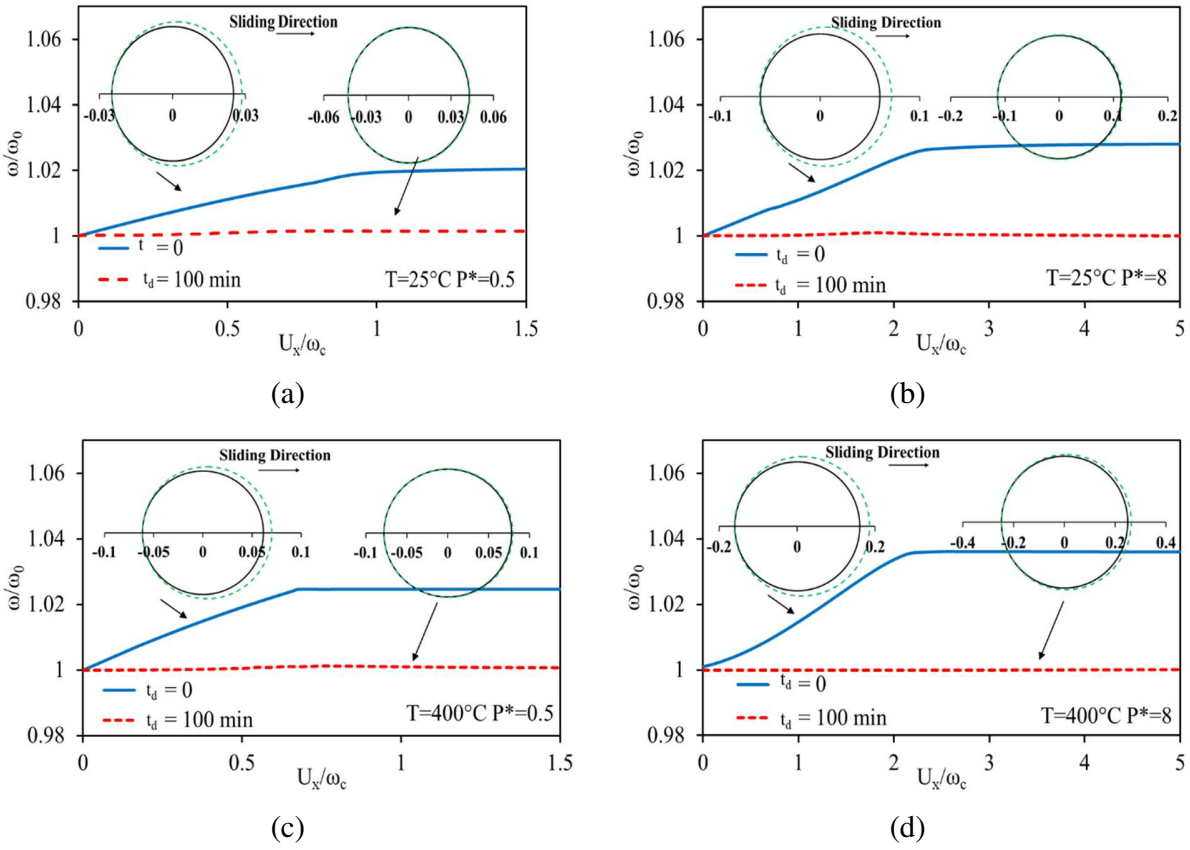

Fig. 4 *Dimensionless normal interference versus dimensionless tangential displacement before (blue solid line) and after (orange dashed line) tangential displacement: (a)* $P^* = 0.5$*, T=25°C and (b)* $P^* = 8$ *T=25°C, (c)* $P^* = 0.5$*, T=400°C and (d)* $P^* = 8$ *T=400°C.*

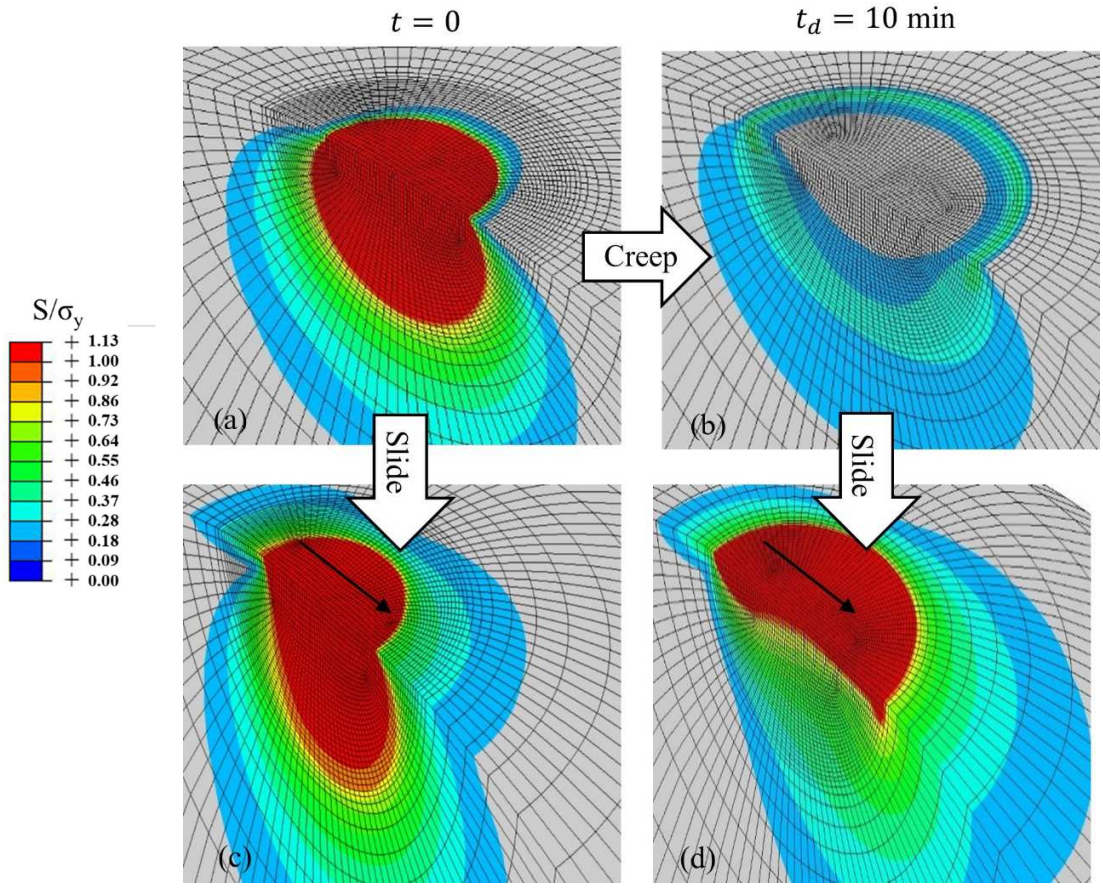

Fig. 5 *Development of dimensionless von Misses stresses, S/σ_y, under a normal load of P*=8 at 400 °C for a) $t = 0$ and b) $t = 10$ min prior to tangential loading; c) sliding inception after zero dwell time and d) sliding inception after t_d = 10 min dwell time (black arrow shows sliding direction in (c) and (d)).*

Fig. 6 shows the effect of dwell time on the evolution of dimensionless contact areas, A/A_0, at different loads and temperatures where A_0 is the initial contact area right after the application of normal loading. It can be observed that by increasing the temperature and dwell time, the difference between the dimensionless contact areas for different loadings at each dwell time, increases and become more noticeable. As temperature increases, the contact evolution-time relation changes from a semi-linear to a power-law curve in which the rate of change, becomes almost constant after some time. The steady state condition is reached earlier for higher temperatures. This is in agreement to the contact area results of Brot et al. (Brot et al., 2008) and Goedecke et al. (Goedecke and Mock, 2009). It should be emphasized that simulations were

stopped when the ratio of contact radius over asperity radius (a/R) increased beyond 0.412 as discussed (Jackson and Green, 2003). Also, for few cases in high loads and dwell times, numerical convergence was challenging without easing the ES and creep tolerance, in which NNs prediction is used to extend the results. Whenever applicable the black lines show the extension of FE analysis using NNs predictions. It should be emphasized that the extrapolatory results of NNs were only used for limited cases where FE simulations did not converge. Based on the FE results for the contact area and COF evolutions, we expect that the curve would continue smoothly and that is actually what was predicted by the NNs for out-of-the-range data. In addition, the training points and test prediction points were selected randomly from the FE results where there was no relation among the selected points.

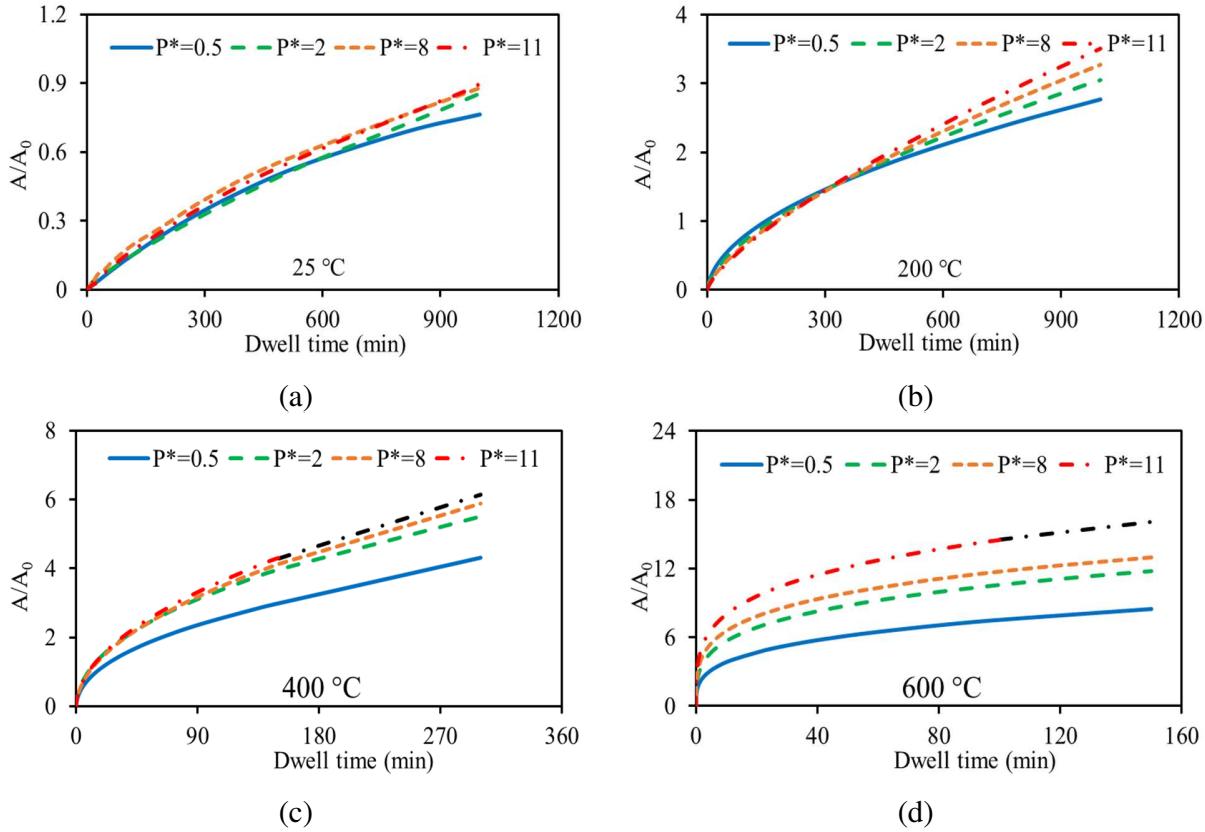

Fig. 6 *Evolution of contact area with dwell time for different loads, P*, from 25 °C to 600 °C. (As the dimensionless radius of contact ratio, a/R, reaches 0.4 simulations are stopped and results are extended using NNs by a black line)*

Fig. 7 shows the evolution of total COF, μ, for different temperatures and increasing increments of dimensionless displacement, U_x/ω_c under a constant load of $P^* = 8$. Here U_x is displacement

along the "x" axis as shown in **Fig. 1** and ω_c is the critical interference based on Hertzian calculation (Eq. 4). The COF is calculated by dividing the maximum tangential friction force, Q_{max} by the constant normal load. In all temperatures with an increase of dwell time, the COF increases, while the rate of increase is more dependent on temperature rather than dwell time. For example, at 600 °C, with 10 min of holding, COF increased 4 times while at 25 °C with 1000 min of holding, COF increased 1.5 times.

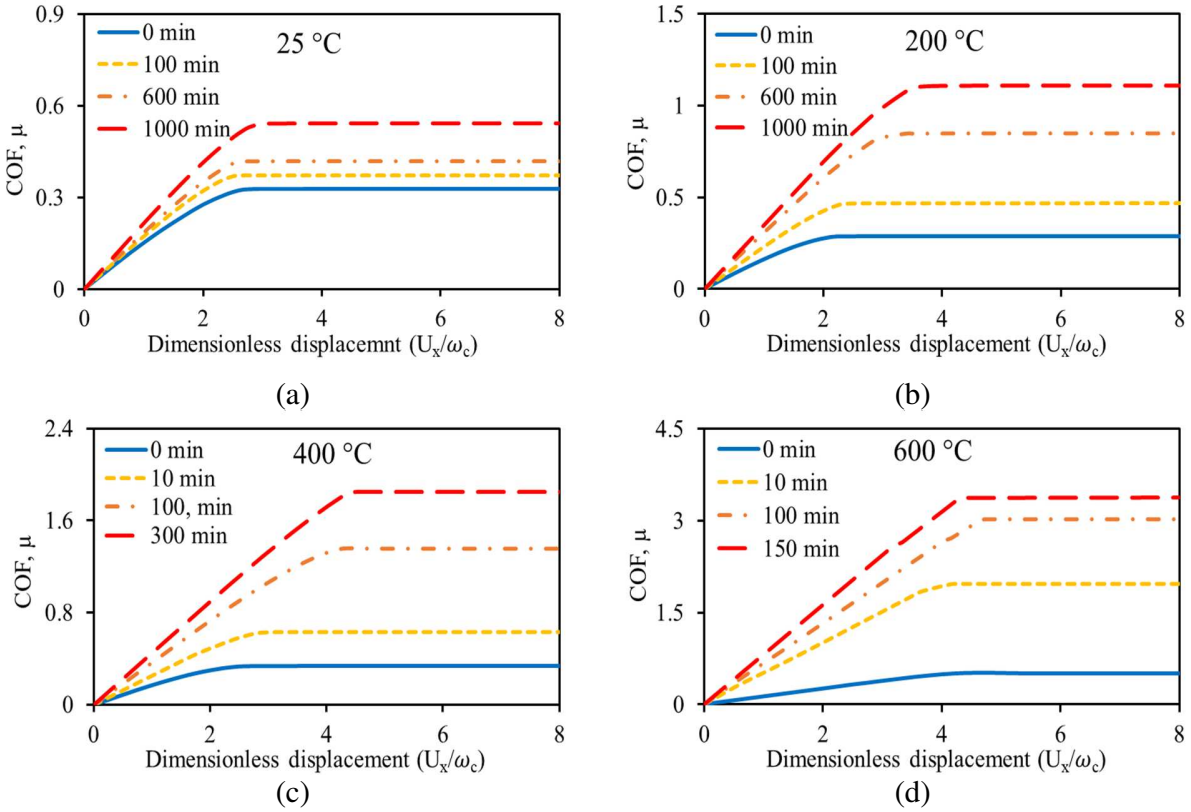

Fig. 7 COF versus dimensionless displacement for different dwell times and temperatures for the load of $P^* = 8$

To better show this rate of increase, a comparison between maximum COF (at the verge of sliding) at selected temperatures is presented in Fig. 8: Showing that by increasing the dwell time and temperature, the total COF increases. The effect of temperature is more significant at temperatures higher than 200 °C, which is related to higher creep rate measured for oxide IN617 at higher temperatures in comparison to room temperature (Salari et al., 2020), increasing the contact area (Fig. 6) and relaxing the contact pressure (Fig. 5). With an exception for 600 °C, where oxides were observed to exhibit considerable softening, no significant change with temperature is seen for dwell time of zero (instantaneous COF), primarily due to the fact that

time independent material properties change proportionately having slight effect on COF with dimensionless nature.

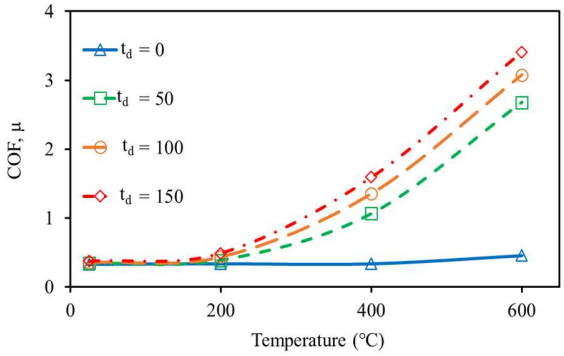

Fig. 8. COF evolution for different temperatures and the normal load of $P^* = 8$ till 150 min of dwell time (t_d).

To better understand the effect of creep deformation on the total COF (μ), we consider it as the summation of the instantaneous COF ($t_d = 0$), defined as, μ_0 and COF increase due to creep, μ_{cr} ($\mu = \mu_0 + \mu_{cr}$). **Fig. 9** presents μ_0 vs. normal load for all temperatures in comparison to WSP. Interestingly, for low dimensionless normal loads and below 400 °C, all the instantaneous COFs show similar behavior for increasing dimensionless loads. It is noted that with different Poisson's ratios, strain hardening and σ_y/E ratio, COF may differ from conventional models (Bhagwat et al., 2017; Brizmer et al., 2007; Wu et al., 2012). Being more ductile at 600 °C, the oxide undergoes considerable plastic deformation with strain hardening before sliding. Thus, it resists sliding at high plastic strains and increasing COF. This is aligned with the COF results reported for Al 2024-T3 as the reference material and with different strain hardening coefficients (Bhagwat et al., 2017). Bhagwat et al. showed that for a linear strain hardening material (Al 2024-T3) with increasing the hardening coefficient the COF increases, however, with increasing dimensionless normal displacement (or dimensionless normal load in our case) the COF for all hypothetical materials decreases and converges asymptotically (Bhagwat et al., 2017). Similarly, harder materials (here T < 400 °C) are unable to achieve a large amount of plastic deformation and show little difference in static COF (Bhagwat et al., 2017).

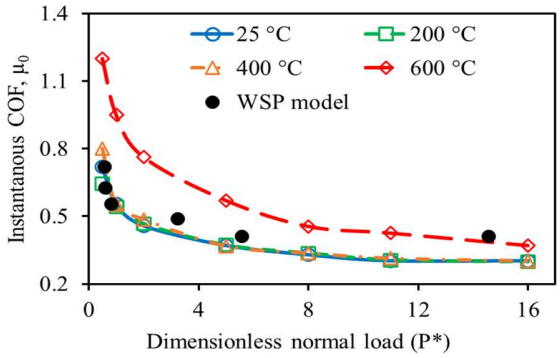

Fig. 9 *Instantaneous COF versus dimensionless tangential displacement for IN617 for different loads and temperatures compared with Wu et al* (Wu et al., 2012).

Fig. 10 presents (μ_{cr}) for the selected temperatures and dimensionless loads. For all temperatures, an increase in μ_{cr} can be observed with dwell times. However, their difference gradually decreases with increasing temperature and load. This can be related to increasing plastic deformation and hardening at the contact for loads beyond the critical load, L_c. The equivalent stress at the contact is higher compared to lower loads which decreases further deformation of the contact and required less tangential force to reach the sliding threshold (Malamut et al., 2009; Phani et al., 2017; Phani and Oliver, 2016). Similarly, at higher temperatures the yield strength decreases, which reduces the tangential force required to reach the sliding threshold.

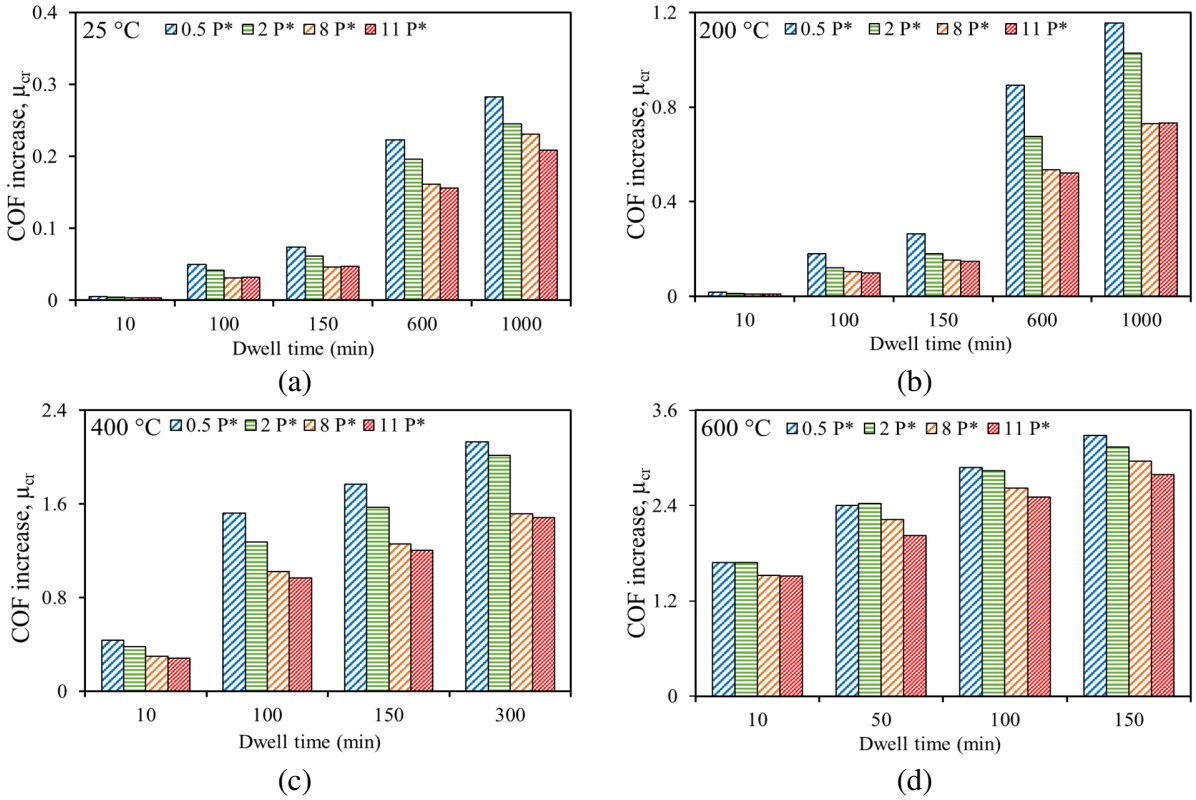

Fig. 10 *Maximum COF increase due to creep during dwell time for the oxide of aged IN617 at different dwell times and maximum loads for (a) 25 °C (b) 200 °C (c) 400 °C (d) 600 °C.*

The total COF versus the dimensionless normal load for different temperatures is presented in **Fig. 11**. It can be seen that as the load increases, the total COF decreases and for all temperatures there exist a threshold (approximately $P^* = 10$) beyond which COF levels off, and become independent of load. To better compare this threshold COF for each temperature, it is presented for different temperatures and loads in **Fig. 12**. As seen, threshold COF changes noticeably for temperatures higher than 400 °C with dwell times. Based on these results, it can be argued that at higher temperatures like 950 °C if phase transformation does not happen for the oxide, the COF will not surpass 2.8 for dwell times of more than 150 min.

It is clear that after considerable dwell time, the COF of the asperity increases due to the stress relaxation in the contact as well as the evolution of the contact area during creep. While a COF of 3 seems to be very high and somewhat exaggerated, values of more than 2 were reported even for kinetic COF of IN617 measured through the pin-on-disk configuration at 800 °C (Rahman et al., 2019, 2018). The high COF can be related to the mechanical properties of the oxide and more

1 importantly significant creep (Salari et al., 2020). This high COF was also seen for hypothetical
2 materials with linear strain hardening (Bhagwat et al., 2017).

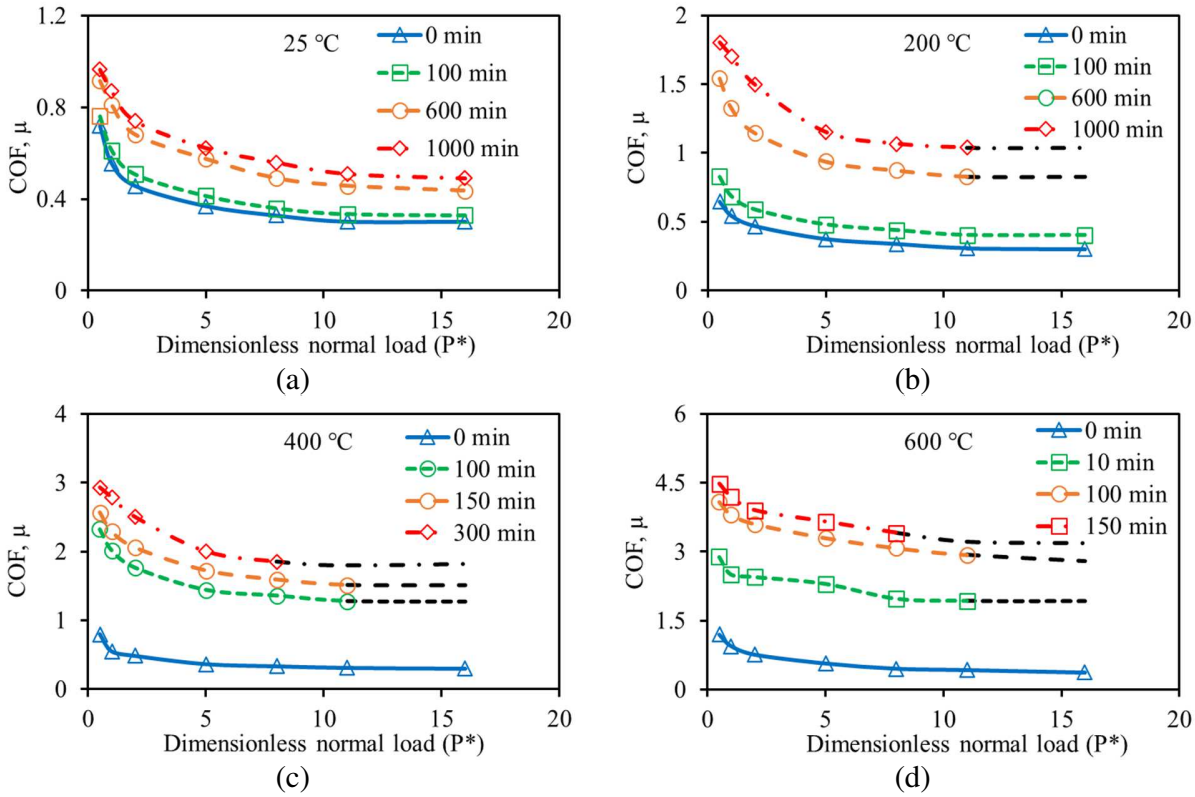

Fig. 11 *Total static COF versus the dimensionless normal load for (a) 25 °C (b) 200 °C (c) 400 °C (d) 600 °C*

3

4

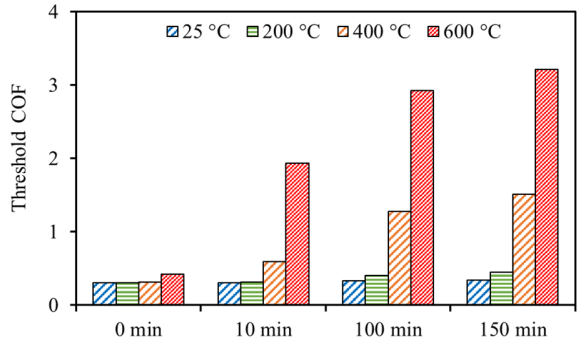

Fig. 12 *Threshold COF for different temperatures and dwell times till 150 min.*

5

4.3 Predictive neural network model

In this work, we trained four separate models to analyze the sensitivity of the NNs for dimensionless contact area and COF to the input parameters (dwell time, temperature, load). The first model is trained by all three input features. The final results for the dimensionless contact area have a MSE of 1.16 and RE of 0.29. The MSE of the NNs for the COF is 0.19 and its RE is 0.18. To compare the performance of the NNs for the two data sets (COF and contact area) RE is a better and consistent measure and is used below. For the second model, we eliminated the temperature feature from the inputs, whereas the REs increase to 2.94 and 0.60 for the dimensionless contact area and COF, respectively, showing that the temperature has a significant role in training a more accurate model for contact area, which is also in agreement with the observations in **Fig. 6**. For the third and fourth models, we eliminated the load and time features from the inputs and obtained the results of REs as follows for the dimensionless contact area and COF, respectively: 0.59 & 0.18 (for the load) and 0.80 & 0.79 (for the time). Related to the work here, an interesting study was done by (Bessa et al., 2017) based on global sensitivity analysis to investigate the effect of each input along with the combine effect of parameters (two inputs, three inputs, etc.). The provided sensitivity analysis, discussed in the current study, follows the same concept where the effect of eliminating each input (load, dwell time and temperature) along with partial effect of other combined inputs (here, two inputs) were explored, concurrently. **Fig. 13** quantitatively shows the relative importance of each input.

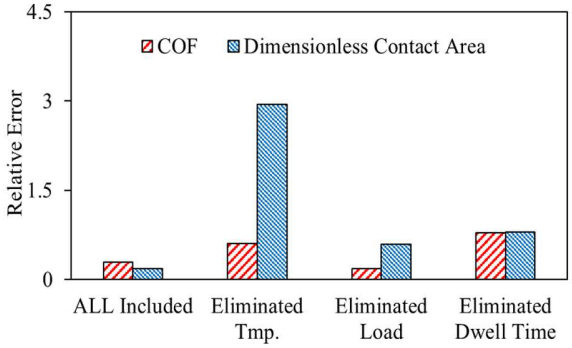

Fig. 13 *Sensitivity analysis of each eliminated parameter on contact area and COF to quantitatively determine the relative importance of the inputs.*

The NNs approach was also deployed on each studied temperature separately and the RE was calculated. **Table 3** shows the relative error (RE) calculated for the COF data set as the

temperature increases. The RE is relatively higher for lower temperatures. One possibility might be the much larger contact area at high temperatures that lowers the sensitivity of the FE model on input parameters.

Table 3 *RE calculated for each temperature*

Temperature (°C)	25	200	400	600
RE	0.30	0.25	0.17	0.18

Fig. 14 shows how well the models performed in predicting the test set for the cases of COF, and dimensionless contact area. When training the neural network, we divided the data into two sets: training, and test. The model is trained on the training data and is evaluated on test data to see how well a fully defined and trained model can work on data entries that are not utilized in the training process. This evaluation is to make sure the NN model can perform well on the data training but does not underperform when encountering unseen data. Please note that here we have three input variables for our prediction model. However, the generality of the proposed technique and the utilization of NNs make it easily possible to expand to any contact problem with accurate predictions even having several input variables and high nonlinearity which cannot be achieved by curve-fitting techniques. In the general context of contact mechanics and tribology, the NNs make it now possible to expands to models where several input parameters are involved. For example, effects of geometry, coating thickness, graded materials, viscoelasticity, high strain rate, and other highly nonlinear mechanical/material properties can be predicted and framed using NNs. It should also be added that simple regression-based expressions were not able to predict observed behaviors (especially for contact area) accurately with reasonable level of error and complexity. This necessitates introducing different sections and ranges in which empirical equations can be fitted to. To further explore this, we followed the simple framework presented by the MKE for the COF of PTFE and expanded it using nonlinear regression analysis to provide a relatively true fit to the FE results of current aged IN617 surface contact (Malamut et al., 2009) (see Section S2 in SI document for the empirical equations). The MSE for COF was obtained to be 1.015 which is much higher than the MSE of the NNs (0.19). A similar method was also attempted for dimensionless contact area where the MSE of 1.54 (compared to 1.16 from NNs training) is obtained. To further evaluate the NNs outcome, we also

conducted the Gaussian process (See Section S3 in the SI file). For the case of Gaussian process, the results were better than the analytical (curve-fit) model, but generally less accurate compared to the NNs. The relative error for Gaussian was 0.49 for contract area prediction and 0.12 for COF compared to that of NNs: 0.29 for contract area prediction and 0.18 for COF.

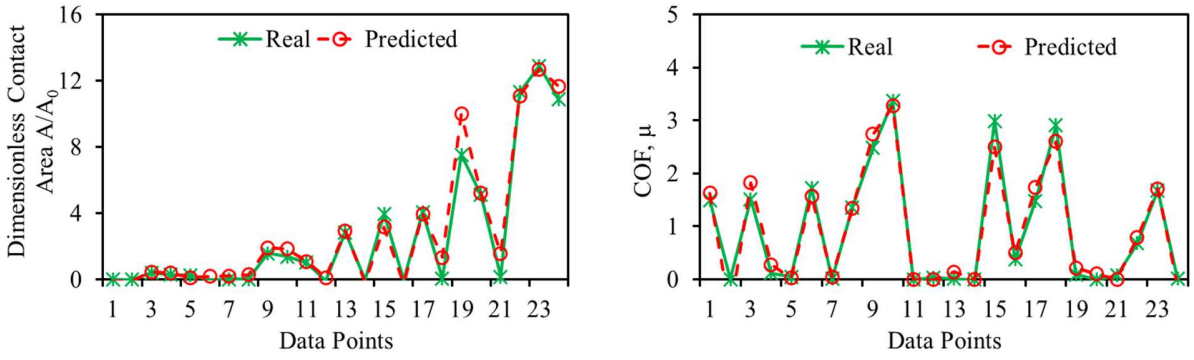

(a) (b)

Fig. 14 Predicted (a) dimensionless contact area and (b) COF for different loads and temperatures using NN modeling in comparison with real data points from FE simulations.

5. Conclusion

The contact creep and COF of the oxide of aged IN617 is investigated numerically using FE simulation. Based on the contact area and total COF results, a predictive NN algorithm is utilized to predict the contact and friction behavior for different normal loads, dwell times, and temperatures. Material properties of the oxide for different temperatures are obtained from the authors' previous study in which elevated temperature nanoindentation was performed on the cross-section of the oxide layer (Salari et al., 2020). The main findings from this study are:

- Maximum shear stress at the contact shows a curved shape, due to work hardening at the contact, while the minimum point at the contact is the last that reaches the sliding criterion;
- Normal interferences during the application of tangential loading show no noticeable change after dwell time for all loads, which is related to loss of the plastic zone under the normal load and substantial stress relaxation during creep deformation;

- Behavior of contact evolution with time changes from a semi-linear to a power-law curve with increasing temperature in which the rate of change, becomes almost constant after some time;
- Increasing normal contact load decreases COF at all temperatures and for all dwell times, which follow general observations for asperity static COF;
- Due to high nonlinearity of the COF and contact area with input parameters, achieving an *accurate* and *simple* expression to fit the data is challenging. NNs can easily and readily solve these issues.
- Based on the sensitivity analysis performed by NNs, the prediction model for the contact area is highly sensitive to temperature and to less extend dwell time. The COF prediction model is equally dependent on temperature and dwell time. NNs approach is a powerful tool for predicting both the contact area and COF for the selected range and beyond. The only challenge to be considered is to provide enough data for the range of training.
- Understanding the effect of creep on the COF of contacting parts especially at high temperatures are essential for developing tribological models of the surfaces. This model can be utilized for the prediction of multi-asperity rough surfaces using, for example, statistical or fractal-based model; and
- The utilization of NNs can be expanded for predicting COF and contact area based on various mechanical, geometrical, load, and dwell times providing a more realistic prediction of surface behavior for various contact mechanics and tribology problems.

Acknowledgment

This study was supported in part by the U.S. Department of Energy (DOE) under NEUP Project 16-10732 and also partially funded by George Mason University. The authors would also thank the Office of Research Computing (ORC) team at George Mason University for providing computational facility.

6. References:

Beheshti, A., Khonsari, M.M., 2014. On the contact of curved rough surfaces: contact behavior and predictive formulas. J. Appl. Mech. 81. https://doi.org/10.1115/1.4028426

Beheshti, A., Khonsari, M.M., 2012. Asperity micro-contact models as applied to the deformation of rough line contact. Tribol. Int. 52, 61–74. https://doi.org/10.1016/j.triboint.2012.02.026

Behnia, F., Mirzaeian, A., Sabokrou, M., Manoj, S., Mohsenin, T., Khasawneh, K.N., Zhao, L., Homayoun, H., Sasan, A., 2020. Code-Bridged Classifier (CBC): A Low or Negative Overhead Defense for Making a CNN Classifier Robust Against Adversarial Attacks. arXiv Prepr. arXiv2001.06099.

Bessa, M.A., Bostanabad, R., Liu, Z., Hu, A., Apley, D.W., Brinson, C., Chen, W., Liu, W.K., 2017. A framework for data-driven analysis of materials under uncertainty: Countering the curse of dimensionality. Comput. Methods Appl. Mech. Eng. 320, 633–667. https://doi.org/10.1016/J.CMA.2017.03.037

Bhagwat, P., Sista, B., Vemaganti, K., 2017. A computational study of the effects of strain hardening in micro-asperity friction models. Tribol. Lett. 65, 154.

Borjali, A., Monson, K., Raeymaekers, B., 2019. Predicting the polyethylene wear rate in pin-on-disc experiments in the context of prosthetic hip implants: Deriving a data-driven model using machine learning methods. Tribol. Int. 133, 101–110.

Brizmer, Kligerman, Etsion, 2007. Elastic--plastic spherical contact under combined normal and tangential loading in full stick. Tribol. Lett. 25, 61–70.

Brot, C.C., Etsion, I., Kligerman, Y., 2008. A contact model for a creeping sphere and a rigid flat. Wear 265, 598–605.

Cabet, C., Terlain, A., Lett, P., Guetaz, L., Gentzbittel, J., 2006. High temperature corrosion of structural materials under gas-cooled reactor helium. Mater. Corros. 57, 147–153.

Chang, W.R., Etsion, I., Bogy, D.B., 1988. Static friction coefficient model for metallic rough surfaces. J. Tribol. 110, 57–63. https://doi.org/10.1115/1.3261575

Deng, L., Li, X., 2013. Machine learning paradigms for speech recognition: An overview. IEEE Trans. Audio. Speech. Lang. Processing 21, 1060–1089.

Eriten, M., Polycarpou, A.A., Bergman, L.A., 2012. A physics-based friction model and integration to a simple dynamical system. J. Vib. Acoust. Trans. ASME 134, 1–9. https://doi.org/10.1115/1.4006182

Feng, G., Ngan, A.H.W., 2002. Effects of creep and thermal drift on modulus measurement using depth-sensing indentation. J. Mater. Res. 17, 660–668.

Frydrych, K., Karimi, K., Pecelerowicz, M., Alvarez, R., Dominguez-Gutiérrez, F.J., Rovaris, F., Papanikolaou, S., 2021. Materials Informatics for Mechanical Deformation: A Review of Applications and Challenges. Mater. 2021, Vol. 14, Page 5764 14, 5764. https://doi.org/10.3390/MA14195764

Goedecke, A., Mock, R., 2010. Transient friction effects due to variable normal load in a multi-scale asperity-creep friction model, in: STLE/ASME 2010 International Joint Tribology Conference. pp. 337–339.

Goedecke, A., Mock, R., 2009. Creep relaxation of an elastic-perfectly plastic hemisphere in fully plastic contact. J. Tribol. 131, 1–10. https://doi.org/10.1115/1.3081978

Greenwood, J.A., Williamson, J.B.P., Greenwood, Williamson, 1966. Contact of nominally flat surfaces. Proc. R. Soc. London. Ser. A. Math. Phys. Sci. 295, 300–319. https://doi.org/10.1098/rspa.1966.0242

Hahnloser, R.H.R., Sarpeshkar, R., Mahowald, M.A., Douglas, R.J., Seung, H.S., 2000. Digital selection and

analogue amplification coexist in a cortex-inspired silicon circuit. Nature 405, 947–951.

Hashash, Y.M.A., Jung, S., Ghaboussi, J., 2004. Numerical implementation of a neural network based material model in finite element analysis. Int. J. Numer. Methods Eng. 59, 989–1005. https://doi.org/10.1002/NME.905

He, K., Zhang, X., Ren, S., Sun, J., 2016. Deep residual learning for image recognition, in: Proceedings of the IEEE Conference on Computer Vision and Pattern Recognition. pp. 770–778.

Heidari, M., Jones, J.H.J., Uzuner, O., 2021. An empirical study of machine learning algorithms for social media bot detection, in: 2021 IEEE International IOT, Electronics and Mechatronics Conference, IEMTRONICS 2021 - Proceedings. Institute of Electrical and Electronics Engineers Inc. https://doi.org/10.1109/IEMTRONICS52119.2021.9422605

Jackson, R.L., Green, I., 2005. A finite element study of elasto-plastic hemispherical contact against a rigid flat. J. Tribol. 127, 343–354. https://doi.org/10.1115/1.1866166

Jackson, R.L., Green, I., 2003. A Finite Element Study of Elasto-Plastic Hemispherical Contact, in: International Joint Tribology Conference. pp. 65–72. https://doi.org/10.1115/2003-TRIB-0268

Jain, A.K., Mao, J., Mohiuddin, K.M., 1996. Artificial neural networks: A tutorial. Computer (Long. Beach. Calif). 29, 31–44.

Kasem, H., Etsion, I., 2014. Experimental study of the effect of dwell time and normal load on static friction in creeping elastic-plastic polymer spherical contact. Wear 309, 139–145. https://doi.org/10.1016/j.wear.2013.11.006

Khourshid, A., El-Kassas, A., of, I.S.-I.J., 2015, undefined, n.d. Integration between artificial neural network and responses surfaces methodology for modeling of friction stir welding. academia.edu.

Kingma, D.P., Ba, J., 2014. Adam: A method for stochastic optimization. arXiv Prepr. arXiv1412.6980.

Klocke, F., Zeis, M., Klink, A., Veselovac, D., 2013. Experimental research on the electrochemical machining of modern titanium-and nickel-based alloys for aero engine components. Procedia Cirp 6, 368–372.

Kogut, L., Etsion, I., 2003. A semi-analytical solution for sliding inception of a spherical contact. J. Tribol. 125, 499–506. https://doi.org/10.1115/1.1538190

Kumar, A., Irsoy, O., Ondruska, P., Iyyer, M., Bradbury, J., Gulrajani, I., Zhong, V., Paulus, R., Socher, R., 2016. Ask me anything: Dynamic memory networks for natural language processing, in: International Conference on Machine Learning. pp. 1378–1387.

Malamut, S., Kligerman, Y., Etsion, I., 2009. The effect of dwell time on the static friction in creeping elastic--plastic polymer spherical contact. Tribol. Lett. 35, 159–170.

Mindlin, and Deresiewicz, H., 1953. Elastic Spheres in Contact Under Varying Oblique Forces. J. Appl. Mech. Trans. ASME 20, 327–344.

Moore, A.C., Tabor, D., 1952. Some mechanical and adhesive properties of indium. Br. J. Appl. Phys. 3, 299.

Phani, P.S., Oliver, W.C., 2016. A direct comparison of high temperature nanoindentation creep and uniaxial creep measurements for commercial purity aluminum. Acta Mater. 111, 31–38. https://doi.org/10.1016/j.actamat.2016.03.032

Phani, P.S., Oliver, W.C., Pharr, G.M., 2017. On the Measurement of Power Law Creep Parameters from Instrumented Indentation. JOM 69, 2229–2236.

Rabinowicz, E., Tanner, R.I., 1966. Friction and wear of materials.

Rahman, M.S., Ding, J., Beheshti, A., Zhang, X., Polycarpou, A.A., 2019. Helium Tribology of Inconel 617 at Elevated Temperatures up to 950° C: Parametric Study. Nucl. Sci. Eng. 1–15.

Rahman, M.S., Ding, J., Beheshti, A., Zhang, X., Polycarpou, A.A., 2018. Elevated temperature tribology of Ni

alloys under helium environment for nuclear reactor applications. Tribol. Int. 123, 372–384.

Rezvanian, O., Brown, C., Zikry, M.A., Kingon, A.I., Krim, J., Irving, D.L., Brenner, D.W., 2008. The role of creep in the time-dependent resistance of Ohmic gold contacts in radio frequency microelectromechanical system devices. J. Appl. Phys. 104. https://doi.org/10.1063/1.2953072

Sakaba, N., Hamamoto, S., Takeda, Y., 2010. Helium chemistry for very high temperature reactors. J. Nucl. Sci. Technol. 47, 269–277.

Salari, S., Beheshti, A., 2021. Asperity-based contact and static friction with provision for creep: A review. Surfaces and Interfaces. https://doi.org/10.1016/j.surfin.2021.101144

Salari, S., Rahman, M.S., Beheshti, A., Polycaropou, A.A., 2022. Elevated temperature nanoscratch of Inconel 617 Superalloy. Mech. Res. Commun. 103875. https://doi.org/10.1016/J.MECHRESCOM.2022.103875

Salari, S., Rahman, M.S., Polycarpou, A.A., Beheshti, A., 2020. Elevated temperature mechanical properties of Inconel 617 surface oxide using nanoindentation. Mater. Sci. Eng. A 788, 139539. https://doi.org/10.1016/j.msea.2020.139539

Sattari Baboukani, B., Ye, Z., G Reyes, K., Nalam, P.C., 2020. Prediction of Nanoscale Friction for Two-Dimensional Materials Using a Machine Learning Approach. Tribol. Lett. 68, 1–14.

Senatore, A., D'Agostino, V., Di Giuda, R., Petrone, V., 2011. Experimental investigation and neural network prediction of brakes and clutch material frictional behaviour considering the sliding acceleration influence. Tribol. Int. 44, 1199–1207.

Smith, M., 2017. ABAQUS/Standard User's Manual, Version 2017. Simulia.

Spurr, R.T., 1955. Creep and static friction. Br. J. Appl. Phys. 6, 402–403. https://doi.org/10.1088/0508-3443/6/11/306

Stanford, M.K., 2007. A review of tribomaterial technology for space nuclear power systems.

Tabor, D., 1981. Friction—the present state of our understanding.

Thankachan, T., Soorya Prakash, K., Kamarthin, M., 2018. Optimizing the tribological behavior of hybrid copper surface composites using statistical and machine learning techniques. J. Tribol. 140.

Wright, R.N., 2006a. Kinetics of gas reactions and environmental degradation in NGNP helium. Citeseer.

Wright, R.N., 2006b. Summary of studies of aging and environmental effects on Inconel 617 and Haynes 230.

Wu, A., Shi, X., Polycarpou, A.A., 2012. An elastic-plastic spherical contact model under combined normal and tangential loading. J. Appl. Mech. 79, 51001. https://doi.org/10.1115/1.4006457

Zhang, Y., Mohanty, D.P., Seiler, P., Siegmund, T., Kruzic, J.J., Tomar, V., 2017. High temperature indentation based property measurements of IN-617. Int. J. Plast. 96, 264–281.

Zheng, Y., Rahman, M.S., Polycarpou, A.A., 2020. Self-welding of Inconel 617 under high-pressure-high-temperature conditions for nuclear reactors. Nucl. Eng. Des. 110941.